Measurement and simulation of spontaneous Raman scattering spectra in high-pressure, fuel-rich H$_2$–air flames

JUN KOJIMA[¶] AND QUANG-VIET NGUYEN[§]

NASA Glenn Research Center, Cleveland OH 44135

[¶] NRC Research Associate, MInstP, Jun.Kojima@grc.nasa.gov, Fax: (440) 962-3120, Phone: (440) 962-3095
[§] Correspondence: Quang-Viet.Nguyen@grc.nasa.gov, Fax: (216) 433-5802, Phone: (216) 433-3574

Abstract

Rotational vibrational spontaneous Raman spectra (SRS) of H$_2$, N$_2$, and H$_2$O have been measured in H$_2$–air flames at pressures up to 30 atm as a first step towards establishing a comprehensive Raman spectral database for temperatures and species in high-pressure combustion. A newly developed high-pressure burner facility provides steady, reproducible flames with a high degree of flow precision. We have obtained an initial set of measurements that indicate the spectra are of sufficient quality in terms of spectral resolution, wavelength coverage, and signal-to-noise ratio for use in future reference standards. The fully resolved Stokes and anti-Stokes shifted SRS spectra were collected in the visible wavelength range (400 – 700 nm) using pulse-stretched 532 nm excitation and a non-intensified CCD spectrograph with a high-speed shutter. Reasonable temperatures were determined via the intensity distribution of rotational H$_2$ lines at stoichiometry and fuel-rich conditions. Theoretical Raman spectra of H$_2$ were computed

using a semi-classical harmonic-oscillator model with recent pressure broadening data and were compared with experimental results. The data and simulation indicated that high-J rotational lines of H_2 might interfere with the N_2 vibrational Q-branch lines, and this could lead to errors in N_2-Raman thermometry based on the line-fitting method. From a comparison of N_2 Q-branch spectra in lean H_2 low-pressure (1.2 atm) and high-pressure (30 atm) flames, we found no significant line-narrowing or -broadening effects at the current spectrometer resolution of 0.04 nm.

1. Introduction

In light of the fact that today's advanced gas turbine combustors or internal combustion engines are modeled with increasingly sophisticated numerical codes that include the effects of finite-rate turbulence-chemistry interactions, it is imperative that an experimental check be performed on these codes whenever a new model is incorporated. Such codes have to be validated by experiment, i.e. they have to go through the so-called code validation process, before they can be relied upon to predict combustion processes accurately. Non-intrusive laser diagnostics play a major role in this code validation process. Particularly, spontaneous Raman scattering (SRS) has been a popular method of probing flames because it is one of the few techniques that provides quantitative multi-species, point measurements in turbulent reacting flows [1]. Although spontaneous Raman signals are inherently very weak, one can expect high quality SRS data with good signal-to-noise ratio (SNR) using either UV laser excitation [2-7] or visible laser excitation in conjunction with a high-performance optical setups that utilize a pulse-stretcher and high-sensitivity detection methods [8-10]. Thus, even single-shot measurements with good SNR can be achieved in turbulent flames using SRS. The single-shot nature of the data acquired from SRS point measurements in flames is often collected over a period of time to form a 'scatter plot' of concentration and/or temperature versus mixture fraction that can be used to validate computational models of turbulent combustion [11-14]. The choice of using SRS for turbulent flame diagnostics also provides practical benefit: the ability of working with only a single optical access port in the back-scattered collection mode. This is often useful for industrial applications where the number of optical windows needs to be kept to a minimum.

Although SRS signals are inherently linearly proportional to both species number density and excitation laser energy, a calibration procedure often has to be used to account for spectral interferences or 'cross-talk' between species or to mitigate the effects of laser-induced fluorescence (LIF) interference. Thus, a challenge of using SRS to study turbulent flame is the fact that a complicated calibration procedure to characterize the SRS signal response over a comprehensive range of conditions is required in order to empirically account for the effects of spectral interferences that are a function of temperature, and species concentration. In the past, these calibration procedures have typically relied on one-of-a-kind apparatus [2-14]. The equipment and effort in labor required to produce these calibration data at atmospheric pressure conditions is enormous, often requiring hundreds of flame conditions at different equivalence ratios and using various fuel-oxidizer combinations. Since the setups used in these previous efforts are one-of-a-kind in nature, the calibration data from these setups is not easily convertible into a transferable standard that is suitable for use by others in the combustion diagnostics community. Duplicating such calibrations is prohibitively expensive, and should really be unnecessary if a transferable standard were to be developed and adopted. Thus, it is critical to provide a transferable Raman calibration standard that is setup-independent.

Despite the numerous studies that use SRS in combustion studies, few studies have been made to carefully examine the SRS spectral response in *high-pressure* combustion systems. Examples of the few SRS studies at high-pressures include: high-pressure research gas turbine combustors [15], internal combustion engines [16-17], and rocket engines [18] have been reported. Work describing high-pressure gas cell studies have also been used to confirm that SRS signals are linearly proportional to gas density [19]. However, these previous studies do not address the fundamental spectroscopic aspects of Raman spectra in high-pressure flames. A recent study that does address the fundamental spectroscopy of Raman scattering in a 5-bar laminar CH_4/air flames is described by Cheng *et al* [20]. In this study they demonstrated that temperature measurement via N_2 Stokes spectral shape could be performed. However, we are unaware of a previous study that is aimed at providing a transferable Raman spectral database applicable to species/temperature measurements in high-pressure flames including the effects of spectral interferences among different molecular spectra.

The goal of our research is to investigate the entire Raman spectral response for quantitative, multi-species information of molecular density and temperature in high-pressure combustion environments. Toward this aim, we developed a precisely controlled high-pressure gaseous burner with which to employ advanced Raman diagnostics. Measurement of the full visible spectrum of the Raman scattering from a H_2–air rich flame at elevated pressures up to 30 atm was made to demonstrate our system performance. The theoretical spectra of pure rotational H_2 Raman, and vibrational H_2 Raman calculated including pressure-broadening effects were then compared to the experimental data to provide further insight into the spectral response of SRS in high-pressure flames. Finally, we determined the temperature and examine interferences between different molecular spectra.

2. Modeling of Raman Spectra

2-1. Raman Cross Section

We modeled the Raman scattering spectra following a semi-classical anharmonic oscillator formalism. According to Placzek's polarization theory of the Raman effect, the corresponding differential Stokes-shifted Raman scattering cross-section per molecule at thermal equilibrium is given by [1,21]:

$$\left(\frac{\partial \sigma}{\partial \Omega}\right)_{i \to f} = C(v_0 - v_k)^4 g_i \frac{\exp(-E_i / kT)}{Q(T)} \Phi .$$

(1)

Here, C is the molecule-independent constant; v_0 is excitation light frequency; v_k is molecular frequency associated with the rotation-vibration, or pure rotation transition from the initial state i to final state f; g_i is the total degeneracy; E_i is the energy of the initial state; k is the Boltzmann constant; T is the gas temperature; $Q(T)$ is the total partition function of the molecule at temperature T, which may be written as the sum of rotational partition function and vibrational function [22]; Φ is a factor that represents the molecule-dependent temperature-independent invariant, which is tabulated by Long [21] for every branch of ro-vibrational and pure rotational Raman scattering. Note that Eq. (1) should be multiplied by the factor $(v + 1)b_v^2$ for ro-vibrational Stokes scattering

of diatomic molecules. Here, v is the vibrational quantum number and $b_v{}^2$ is defined as $h/8\pi^2 c v_k$ where h is the Plank constant, and c is the speed of light.

The Raman spectral line positions are given by the molecular rotational or vibrational frequency v_k, and are calculated on the basis of energy conservation. The energy in a vibrational-rotational state (v, J) is expressed as the sum of the vibrational energy term, $G(v)$ and rotational energy term, $F(v,J)$. The anharmonic oscillator model, in which the non-rigid rotator model was applied to take the influence of centrifugal force due to vibration into account, with the proper molecular constants [23] was used to calculate those energy terms for H_2. Detailed expressions of the model have been described in Ref. 22. The Q-branch of ro-vibrational Raman line is much stronger than the O- and S-branches because the polarizability tensor greatly exceeds the anisotropy invariant. So we calculate only the Q-branch of ro-vibrational Raman scattering for diatomic molecule in the present model.

Thus, Raman line frequencies and intensities of ro-vibrational spectrum of H_2 and pure rotational spectrum of H_2 were calculated using the above methodology. In order to permit comparisons of the calculated Raman spectra for each species with experimental data, we calculated the *relative* (but quantitative) intensity by setting the function Φ and the molecule-independent constants at an arbitrary value.

2-2. Line-Shape Model

We used the Voigt profile to model the spectral line-shape of Raman scattering at high pressures. Although the Voigt profile may not be valid in the far wings of spectral lines at very high pressures due to breakdown of the impact approximation [24], we ignore these effects in favor of the Voigt function for its simplicity and the widespread availability of fast algorithms for rapid computation [25].

The Voigt-a and -x parameters are given by the following relations:

$$a(v, J, P, T) = \sqrt{\ln 2}\, \frac{\Delta v_c(P,T)}{\Delta v_G(v, J)}, \qquad (2)$$

$$x(v,J) = 2\sqrt{\ln 2}\,\frac{v - v_k(v,J)}{\Delta v_G(v,J)}. \tag{3}$$

Here, Δv_G is the overall convolution Gaussian width [cm^{-1}] and may be written as

$$\Delta v_G(v,J) = \sqrt{\Delta v_D^{\;2} + \Delta v_{Spec}^{\;\;2}}, \tag{4}$$

where Δv_D is the molecular-dependent Doppler width [cm^{-1}], and Δv_{Spec} is the spectral resolution of the spectrograph as an instrumental function. Δv_c is the collisional broadening full width [cm^{-1}] and $\Delta v_c = 2\gamma P$, where γ is the collisional-broadening coefficient [cm^{-1}/atm] for a gas total pressure P [atm], and temperature T [K].

The collisional-broadening coefficient of H_2 has been studied for H_2 CARS (Coherent anti-Stokes Raman Spectroscopy) thermometry [26-27]. Hussong *et al* [26] provided an effective, polynomial equation for the H_2 collisional broadening coefficient including the inhomogeneous contribution (nonlinear dependence on the perturber concentration) in the binary system H_2-N_2:

$$\tilde{\gamma}_J^0(T,C) = (\gamma_0^{self})_J + (\tilde{\gamma}^{self})_J\,T + (a_1)_J\,C + (a_2)_J\,C^2 + (a_3)_J\,CT + (a_4)_J\,C^2T \tag{5}$$

where $\tilde{\gamma}_J^0$ [cm^{-1}/atm] is the total broadening coefficient as a function of temperature, T and concentration of perturber, C. Here C is defined as N_2 fraction to H_2 under the assumption of H_2-N_2 binary system. All other parameters, $(\gamma_0^{self})_J$, $(\tilde{\gamma}^{self})_J$, $(a_i)_J$ are tabulated for $J = 0$ to 5 in Ref. 26. In the current study, we calculated the H_2 broadening coefficient for each flame condition with Eq. (5). The mole fractions of H_2, and N_2 and adiabatic temperatures were calculated by the NASA-Glenn chemical equilibrium code [28] for air-fuel ratios, and pressures used in the current experiment. Here, the temperature computed by the code is different by a hundred degrees on average from experimentally determined temperatures for each flame condition, but those differences do not result significant errors for the current comparisons with experimental data. Although the collisional-broadening coefficients are transition dependent we used a single-

value, pressure-broadening coefficient since no reasonable database is available for neither v-dependent collisional broadening coefficients, nor for higher J numbers over $J = 7$ which generally appeared over the range of combustion temperature. We then used the coefficient at $J = 3$ in Eq. (5) for all lines in the H_2 spectrum after considering the typical line intensity of H_2 rotational, and ro-vibrational Raman is highest at $J = 3$ ($v = 0$). Since in spontaneous Raman spectra modeling pressure-broadening line-widths have less impact to overall spectrum shape while it is significant in CARS spectra, the use of the single, non-J-dependent broadening coefficient is not critical to spontaneous H_2-Raman thermometry, nor to spectral analysis for the range of pressure in the current study. Experimental spectra will be compared with computational results with these broadening coefficients to evaluate whether if this assumption is practically appropriate. Note that when $\Delta v_{Spec} \gg \Delta v_c$, Voigt-$a$ becomes nearly zero, so a Voigt profile becomes a Gaussian profile.

Finally, the profile of Raman spectra at the temperature (T) and pressure (P) of interest were calculated by integration (sum) of all Voigt lines based on the assumption of the additive approximation. It should be noted that the interaction between different transitions, the so-called line-mixing [29] in Raman spectra of high-pressure gases, was not included in the present model.

In below sections *vib*-H_2 indicates ro-vibrational H_2 Raman spectra and *rot*-H_2 indicates pure rotational H_2 Raman spectra.

2.3 Temperature Determination

There are a couple of ways to determine temperatures from Raman spectra. N_2 Raman thermometry using Stokes/anti-Stokes integrated intensity ratio of vibrational N_2 Q-branch (AS-S method) [30] or spectral line fitting to N_2 Q-branch (N_2 line-fit method) [31] have been well known. H_2 Raman thermometry [32-34] using the line intensity distribution of *rot*-H_2 is a good alternative in H_2 rich flames since *rot*-H_2 has a relatively strong cross-section, and each rotational spectrum is discriminated very well due to relatively large rotational level spacing. Intensity-integration calculations can also be effectively implemented. For this study, H_2 Raman thermometry was used to determine temperatures.

Thermodynamic temperatures can be determined from the measured relative intensities of pure rotational Raman transitions using the relation [33]:

$$\ln[f(J)S(J)] = -F(J)/kT + \text{const}, \tag{6}$$

where $S(J)$ is the rotational Raman integrated intensity, $F(J)$ [cm^{-1}] is the rotational energy. The term $f(J)$ contains J-dependent terms for the Raman intensities, including correction of the rotation-vibration interactions which are significant in hydrogen [32-33],

$$f(J) = \frac{2J+3}{g(J+1)(J+2)} \cdot \frac{1}{1+A(J^2+3J+3)} \left(\frac{v_0}{v_k(J)}\right)^4 : \text{Stokes (S-branch),} \tag{7}$$

$$f(J) = \frac{2J-1}{gJ(J-1)} \cdot \frac{1}{1+A(J^2-J+1)} \left(\frac{v_0}{v_k(J)}\right)^4 : \text{anti-Stokes (O-branch)} \tag{8}$$

where g is the nuclear spin degeneracy factor ($g = 1$ for even J; $g = 3$ for odd J), $A = 4.02 \times 10^{-3}$, and $v_k(J)$ is the experimentally observed Raman line frequency.

3. Experimental Apparatus

3-1. High-Pressure Multi-Jet Burner

A specially designed high-pressure gaseous burner was used to provide a controllable and stable source of combustion products in high-pressure environments for the calibration and development of the quantitative Raman diagnostic technique. Figure 1 shows the assembly diagram of the burner nozzle which consists of a staggered (alternating) tube array, in which an 8 x 8 array of 1.1 mm diameter holes spaced at 2.6 x 2.6 mm are fed by an oxidizer cavity located just underneath the burner surface. Likewise, a 7 x 7 array of 1.1 mm diameter holes located between oxidizer holes are fed by a fuel cavity. Rapid mixing of fuel and oxidizer is enhanced by multiple jets at high velocity from the

tubes which permits the operation of the non-premixed flame to behave as a quasi-premixed flame. The burner produces a region of combustion products directly downstream of the flame with a uniform flow pattern over an approximate 5 x 5 mm zone. The 300 series stainless steel burner face is convectively cooled by both the flow of the ambient temperature air and fuel, and by the conduction of the main burner body. Note that the non-premixed operation can keep the burner surface far below 400 Centigrade, preventing meltdown at high-pressure and high-temperature combustion.

Figure 2 shows a schematic of the high-pressure burner rig and gas flow system. Room-temperature air from a facility compressor provided 30 atm air for cooling. The cooling air is introduced at the bottom of the rig for liner cooling (0.25 lbm/s max.), and also at the upper side as "quenching" (0.20 lbm/s max.). These airflows were controlled by remotely operated regulators using calibrated venturi flow meters. Approximately 10 % or less of the total cooling flow rate of the facility air was used as a purge-air for the optical windows during experiments to prevent water vapor condensation. The flow rate of the purge-air was set via a sonic venturi. The pressure of the burner rig was maintained via the back-pressure valve mounted at the top of the chamber, which is remotely operated by auto-feedback process controller. The rig pressure was varied from 1.2 atm to 30 atm in the present study although the burner rig can operate up to 60 atm. The pressure was stabilized below ± 1 % for each condition. For optical access, the burner rig has four 44 mm thick UV grade fused silica windows with a clear aperture of 85 mm. A burst disk (935 psig) was placed between the pressure chamber and exhaust pipe in case of a hazardous pressure buildup.

The multi-tube burner is mounted inside a high-temperature liner casing inside the rig. Note that the pressure inside the casing is the same as for the rig. A small amount of cooling air is fed into the casing to avoid building up of combustion products around the burner. The oxidizer air and the fuel H_2 were provided by 12-pack cylinder arrays at 150 atm pressure. The flow rates of the air and fuel were precisely controlled within 1 % accuracy using sonic venturi flow meters with computer operated regulators and valves. For the data presented in this paper, the overall equivalence ratio was varied from $\phi = 0.5$ to $\phi = 3.0$. Pressures and overall equivalence ratios of the current five experiments are shown

in Table 1. Measurements were made 25.4 mm above the burner nozzle surface on the center axis located downstream of the actual flame zone.

3-2. Raman Diagnostics

Figure 3 shows a schematic of the Raman scattering measurement apparatus. For Raman excitation an injection seeded, Q-switched Nd:YAG laser provides nominally 1000-mJ, 532-nm pulses (8.4 ns FWHM) at a 10 Hz repetition rate. Although not needed for Raman scattering in general, the injection seeding feature produces a better pulse-to-pulse energy stability with less timing-jitter. The injection-seeded laser line width as stated by the manufacturer is 0.003 cm^{-1}. The pulses are then temporally "stretched" to about 75 ns (FWHM) using a pulse-stretcher [13] based on multiple ring-cavities. The pulse-stretcher has been described in detail [8] and consists of sixteen mirrors and three beam splitter-combiners arranged in a sequential 3-cavity setup to produce an output pulse with approximately 10% of the peak power of the input pulse, while retaining 83% energy throughput efficiency. Figure 4 shows the performance of the laser pulse-stretching system. The reduced peak power prevents laser-induced spark/plasma formation at the probe volume due to the breakdown of the gas dielectric properties under the intense electric field that would otherwise be generated by the tightly focused Q-switched laser pulse. In addition, the pulse-stretcher reduces the possibility of damage to the windows. The dielectric breakdown of air under intense laser power is problematic because air has a negative pressure dependence for the breakdown threshold versus laser power [35]. Even with a pulse-stretcher, spark or plasma formation is still a problem if dust particles or particulates find their way into the laser probe volume. A 750-mm focal lens focuses the output of the pulse-stretcher to the probe volume waist diameter of approximately 1 mm. The effectively double the probe volume energy, the laser beam is back-propagated through the probe volume at a small crossing angle using a 400-mm collimating lens and a right-angle prism.

The vertically polarized Raman scattering is collected at a 90-degree angle relative to the beam-propagation direction using a standard 35-mm format camera lens (85 mm, f/1.4). The collected light is then focused onto a silica optical fiber (400 μm core diameter) that is sheathed in a flexible metal conduit. An electro-

mechanical high-speed shutter [10] synchronized to the 10-Hz laser pulses optically gates the light emerging from the fiber. Although capable of operating at gate widths as short as 9 μs, the shutter system in this study provides a 24 μs gate time (FWHM) with 0.4 μs jitter through a 12 x 0.8 mm clear aperture with an overall 55% optical throughput including fiber transmission losses. The high-speed shutter system reduces the effects of background light interferences by a factor of about 1000 compared to a conventional electro-mechanical leaf shutter. The optically gated light from the shutter is fiber-optically directed using a second 400-micrometer core silica fiber to an axially transmissive visible-wavelength spectrograph (f/1.8) fitted with a holographic notch filter to attenuate the Rayleigh scattering component of the signal by over six orders of magnitude. A volume holographic transmission grating disperses the signal into different wavelengths which are detected by a non-intensified, thermo-electrically cooled (-45 °C), back-illuminated CCD camera (1340 x 400 array, 20 x 20 μm pixels).

The back-illuminated CCD camera and electro-mechanical shutter combination were selected over an intensified CCD camera because it provides better than 90% detector quantum efficiency (QE) with a 200,000 photoelectron dynamic range that is digitized at 16-bits of resolution. The simultaneous requirements of high detector QE and high dynamic range are critical for accurately capturing the full range of weak and strong Raman signals and its background interferences as they appear in high pressure flames. The electronic exposure of the CCD is set at 5 ms (but the actual time exposure limited by the shutter is 24 μs), and the data is binned on-chip over 50 vertical pixels and accumulated over 700 shots to increase SNR. The spectrograph was calibrated in wavelength using a primary standard (Ne and Hg/Ar discharge lamps). The spectral resolution of the standard holographic grating, Δv_{spec}, is determined from the calibration lamp lines (which are much narrower than the spectrograph resolution) over the spectral range of interest. The spectral resolution of the standard grating varied from 18 cm^{-1}/pixel to 20 cm^{-1}/pixel between 540 nm to 700 nm using a 25 μm slit. Alternatively, we also used a high-resolution double-pass holographic grating that provided a spectral resolution of about 1.1 cm^{-1}/pixel at a wavelength of 620 nm. The high-resolution grating was used for the detailed measurements of the N_2 Q-branch spectra. We corrected the spectral intensity

variations in the system due to detector response and wavelength dependent absorption in the entire collection optical train using NIST-traceable fiber-coupled blackbody calibration lamp. This is essential for the accurate determinations of vibrational and rotational population distributions used for temperature measurements.

4. Results and Discussion

4-1. Combustion Temperature

Laser Raman scattering measurements in combustion environments often suffer from background interferences such as flame luminosity and/or laser induced fluorescence of radicals. Removing these interferences is the key to a quantitative analysis. Even though Raman scattering was measured using a pulsed laser with a high-speed shutter system to minimize spontaneous flame emissions and luminosity, a certain level of background was observed in the Raman scattering spectra. To remove this, the flame luminosity was measured without laser excitation and was subtracted from the original signal. This technique is effective for steady flows which we have in this study. However, in non-steady flows, single shot measurements can utilize background subtraction if the background can be represented as a smooth curve that can be numerically fitted based on intensity values in between Raman features of interest. Figure 5 shows the averaged flame-luminescence-subtracted Raman spectra of H_2–air combustion gases in lean to rich conditions at 10 atm. Relative intensities of *rot-*H_2, and *vib-*H_2 increased significantly when the flame became richer ($\phi = 2.0$ and 3.0) while the vibrational Raman spectra of N_2, and H_2O were observed in all conditions. Pure rotational lines of H_2 are clearly observed from the background noise and highly discriminated from each other. It should be noted that those spectra acquired at higher pressure ($P = 20$, and 30 atm) but not shown here had the same tendency but they had higher SNR because of higher density of molecules, thus Raman scattering intensities.

Plots of the integrated intensities of individual Stokes *rot-*H_2 braches for different flame are shown in Fig. 6. Although the energy distribution of Stokes and anti-Stokes transitions can be a good test for an thermal equilibrium only Stokes branches are plotted on the graph since lower-SNR anti-Stokes lines could

reduce the accuracy of temperature measurement. *Rot*-H_2 $S(0)$ and $S(1)$ lines, which were completely or partially overwhelmed by pure rotational N_2/O_2 Raman spectrum, were also not used for the temperature calculation. As seen in Fig. 6 every curve is well approximated with a linear fit, which means the thermal equilibrium was achieved in the hydrogen molecules. Temperatures have been determined via Eq. (6) substituting slopes of linear least-squares fits. The results are shown with the temperature uncertainties in Table 1 for five different experiment cases. For most of the hydrogen flames in this study, temperatures were above 2200 K. The best case (#3) showed 1878 ± 19 K, with only 1 % uncertainty while an averaged uncertainty was 2.4 %. Thus, it is shown that rotational H_2 thermometry via spontaneous Raman scattering provides a reasonable temperature in a rich high-pressure flame. It is worth noting that this temperature measurement technique does not depend on the pressure broadening or narrowing effects because *integrated* intensities of rotational lines are used in the calculation instead of using peak heights.

4-2. Spectral Interference

Spectral interferences among different molecular Raman spectra, i.e. spectral cross-talk, can be a significant problem for Raman scattering measurements in high pressure. In hydrogen flames, generally, there is much less cross-talk compared to hydrocarbon flames because only four molecules, H_2, H_2O, O_2, N_2 are involved. However, in highly rich, high-temperature, high-pressure flames such as in rocket combustors [18,36] cross-talk between these and other molecular species are not negligible. In high-pressure circumstances the cross-talk becomes more complicated since pressure broadening or narrowing effects are also involved. Rotational H_2 Raman lines in lower J numbers below $J = 10$ (350 to 2300 cm^{-1}) are far enough from N_2 Raman spectrum (2330 cm^{-1}) to be discriminated but the $S(10)$ line at 2391 cm^{-1} at temperature over ca. 2000 K becomes strong enough to interfere with N_2. Higher vibrational lines of N_2 spectrum at higher temperature also interfere with the $S(10)$ line of *rot*-H_2. As for *vib*-H_2 higher J lines could interfere with H_2O in higher temperature. These cross-talk should be accounted quantitatively by theoretical means to figure out how

significant they are to measure accurate number densities of those molecules and temperature.

In order to estimate the rate of this cross-talk *rot*-H_2 and *vib*-H_2 spectra for three cases (#2, 4, and 5) were computed and compared with experimental data in Fig. 7, 8, and 10. Note that the computational spectra are not best-fit theoretical curves to the experimental plots but are the theoretical spectra at the experimentally-derived temperature shown in Table 1, under the pressures. In Fig. 7a, 8a, and 9a we found good agreement in the overall shape between experimental *rot*-H_2 spectra and those of theoretical. In the present experiment, the spectral resolution is much larger than the estimated pressure broadening. Therefore the observed good agreement on the Raman spectral width between measured data and calculated does not immediately support the pressure broadening coefficients assumed in the model. Yet these results indicate the model of the pressure-broadening coefficient and the Voigt function used here are practically appropriate to simulate Raman spectra in high-pressure flames at least up to 30 atm. We did not observe much pressure broadening or narrowing in the current low-spectral-resolution system. There are slight differences in the peak heights in those spectra mainly because *J*-dependent broadening coefficients were not considered in the calculations and/or the uncertainty of temperature determination.

As shown in Fig. 7a, we found out a non-negligible spectral interference of $S(10)$ spectrum of *rot*-H_2 at 605 nm with vibrational N_2 Q-branch spectra in this rich hydrogen flame ($\phi = 3.0$). According to the comparison between theoretical result and experimental $S(10)$ branch likely interferes with the third peak of the N_2 spectra, i.e. $(v', v'') = (3, 2)$ band. So the interference should be considered in a popular temperature measurement via N_2 line-fit method while the integrated intensity of $S(10)$ branch is less than 2 % of that of N_2 Q-branch in this case. It should be also noted that this interference possibly becomes more important in higher temperature, richer H_2 flames.

In Fig. 7b, 8b, and 9b theoretical lines were also found to agree well with the experimental *vib*-H_2 spectra, which indicate that the line-shape model for *vib*-H_2 are appropriate and also that rotational temperature and vibrational temperature are at equilibrium in the flames. We also experimentally observed spectral interferences between *vib*-H_2 and H_2O spectra between 660 and 740 nm. The

blue-side tails in the theoretical spectra clearly show the occurrence of such interferences in high-pressure and -temperature flames.

Figure 10 shows experimental N_2 Q-branch spectra at pressures of 1.2, 20, and 30 atm in H_2–air flames of $\phi = 0.5$. Here there would be almost no interference between *rot*-H_2 $S(10)$ spectrum and N_2 Q-branch spectrum since it is a quite lean flame and almost no hydrogen fuel should be left downstream of the flame zone where the data were measured. As seen in Fig. 10 no significant pressure narrowing effects have been observed with the current resolution of 0.04 nm while slight pressure-broadening effects "smooth" the spectrum with increasing of pressure, i.e. the fine structure of the 1.2-atm spectrum disappeared with increasing pressure. This result indicates the line-mixing effect may not be particularly important to N_2 Raman (spontaneous) thermometry in high-pressure hydrogen flames up to 30 atm. This idea is supported by a report in which the line-narrowing and line-shift of the N_2 Q-branch spectrum due to such line-mixing effects at pressures up to 60 atm have been observed by only an order of 10^{-1} cm^{-1} [37]. In contrast, it is also interesting to point out that we have not observed such distinguished, line-mixing-like "overlap" among three peaks of vibrational transitions in our 30-atm H_2–air flames as Cheng *et al* [20] observed in their CH_4–air 4.9-atm high-pressure flames. This difference might be due to the absence of perturbers such as CH_4 and/or other carbon-based molecules. Further investigation on high-pressure CH_4–air flames in our-type of burner is required to clarify such effects. Note that flame temperatures for the three pressures at the same equivalence ratio (0.5) are almost the same according to computational results of NASA-Glenn CEA code, therefore, the factor of temperature on the spectra shape can be neglected in this discussion.

5. Conclusions

A new high-pressure gaseous burner facility and a high-performance spontaneous Raman scattering diagnostics system (Nd:YAG laser based) have been developed to provide a fundamental, comprehensive Raman scattering spectral database for use as a quantitative calibration standard of temperature and species in high-pressure flames. These facilities were shown to provide high-quality Raman data with good SNR and sufficient spectral resolution. As the first

demonstration, the Raman spectrum of H_2–air combustion gases up to 30 atm was measured. The theoretical spectra of pure rotational H_2 Raman and of vibrational H_2 Raman were calculated using a harmonic-oscillator model and a line-shape model (Voigt function) including the recent numbers of pressure-broadening coefficients.

The clear rotational and ro-vibrational Raman spectra of H_2, N_2, H_2O were observed in hydrogen–air flames of 10, 20, and 30 atm. H_2 Raman thermometry via the rotational energy distribution were successfully applied to high-pressure H_2 rich flames. Temperatures derived from this method showed reasonable numbers with an averaged 2.4 % uncertainty.

Theoretical Raman spectra of rotational H_2, and vibrational H_2 at the experimentally-obtained temperatures were calculated. Overall theoretical spectra agreed well with the experimental results and thus the current Raman spectra modeling can be accepted for the combustion diagnostics purpose. From such comparisons of experimental spectra with theoretical, non-negligible spectral interferences between rotational H_2 spectra and N_2 Q-branch, and vibrational H_2 and vibrational H_2O were found in rich ($\phi = 3.0$) H_2–air flames. The interference of $S(10)$ branch of rotational H_2 Raman could cause uncertainty to the common N_2 Raman thermometry via the line-fit method. Finally, no significant spectral narrowing effects was observed in the N_2 Q-branch of 30-atm hydrogen flames at the current spectrometer resolution of 0.04 nm although there was "smoothing" effects due to the collisional broadening.

Acknowledgement

References

[1] C. Eckbreth, *Laser Diagnostics for Combustion Temperature and Species*: 2nd Ed., Gordon and Breach Publishers, The Netherlands, 209-273, (1996).

[2] E. W. Roths, and P. Andresen, "Application of Tunable Excimer lasers to Combustion Diagnostics: a Review," *Appl. Opt.* **36**, 3971-4033, (1997).

[3] E. P. Hassel, "Ultraviolet Raman-Scattering Measurements in Flames by the Use of a Narrow-Band XeCl Excimer Laser," *Appl. Opt.* **32**, 4058-4065, (1993).

[4] M. S. Mansour, and Y.-C. Chen, "Line-Raman, Rayleigh, and Laser-Induced Predissociation Fluorescence Technique for Combustion with a Tunable KrF Excimer Laser," *Appl. Opt.* **35**, 4252-4260, (1996).

[5] Y. Gu, E. W. Rothe, and G. P. Reck, "One-Dimensional Imaging of H_2 Densities and of Temperatures via Rotational Raman Scattering of Narrow-Band, 248 nm, Laser Light," *J. Raman Spectrosc.* **28**, 605-612, (1997).

[6] F. Rabenstein, and A. Leipertz, "One-Dimensional, Time-Resolved Raman Measurements in a Sooting Flame Made with 355-nm Excitation," *Appl. Opt.* **37**, 4937-4943, (1998).

[7] M. Decker, A. Schik, U. E. Meier, and W. Stricker, "Quantitative Raman Imaging Investigations of Mixing Phenomena in High-Pressure Cryogenic Jets," *Appl. Opt.* **37**, 5620-5627, (1998).

[8] J. Kojima, and Q. V. Nguyen, "Laser Pulse-Stretching Using Multiple Optical Ring-Cavities," *Appl. Opt.* **41**, 6360-6370, (2002).

[9] R. S. Barlow, and P. C. Miles, "A Shutter-Based Line-Imaging System for Single-Shot Raman Scattering Measurements of Gradients in Mixture Fraction," *Proc. Combust. Inst.* **28**, 269-277, (2000).

[10] Q. V. Nguyen, "High Speed Electromechanical Shutter for Imaging Spectrographs," NASA Disclosure of New Invention and Technology, LEW17, 175-1, (2001).

[11] M. C. Drake, R. W. Pitz, and M. Lapp, "Laser Measurements on Nonpremixed H_2-Air Flames for Assessment of Turbulent Combustion Models," *AIAA J.* **6**, 905-917, (1986).

[12] R. W. Dibble, A. R. Masri, and R. W. Bilger, "The Spontaneous Raman Scattering Technique Applied to Nonpremixed Flames of Methane," Combust. Flame **67**, 189-206, (1987).

[13] Q. V. Nguyen, R. W. Dibble, C. D. Carter, G. J. Fiechtner and R. S. Barlow, "Raman-LIF Measurements of Temperature, Major Species, OH, and NO in a Methane-Air Bunsen Flame," *Comb. Flame* **105**, 499-510, (1996).

[14] A. R. Marci, R. W. Dibble, R. S. Barlow, "The Structure of Turbulent Nonpremixed Flames Revealed by Raman-Rayleigh-LIF Measurements," *Prog. Energy Combust. Sci.* **22**, 307-362 (1996).

[15] Y. Gu, E. W. Rothe, G. P. Reck, R. J. Locke, R. C. Anderson, Y. R. Hicks, and Q.-V. Nguyen, "One-Dimensional UV-Raman Imaging of a Jet-A-Fueled Aircraft Combustor in a High Temperature and Pressure Test Cell: A Feasibility Study," *Combust. Sci. Technol.* **174**, 199-215, (2002).

[16] P. C. Miles, "Raman Line Imaging for Spatially and Temporally Resolved Mole Fraction Measurements in Internal Combustion Engines," *Appl. Opt.* **38**, 1714-1732, (1999).

[17] M. Knapp, A. Luczak, V. Beushausen, W. Hentschel, P. Manz, and P. Andresen, "Polarization Separated Spatially Resolved Single Laser Shot Multispecies Analysis in the Combustion Chamber of a Realistic SI Engine with a Tunable KrF Excimer Laser," *Proc. Combust. Inst.* **26**, 2589-2596, (1996).

[18] J. A. Wehrmeyer, J. M. Cramer, R. H. Eskridge, and C. C. Dobson, "Developed of Ultraviolet Raman Diagnostics for Rocket Engine Injector Analysis," *J. Prop. Power* **17**, 27-34, (2001).

[19] Y. Gu, Y. Zhou, H. Tang, E. W. Rothe, and G. P. Reck, "Pressure Dependence of Vibrational Raman Scattering of Narrow-Band, 248-nm, Laser Light by H_2, N_2, O_2, CO_2, CH_4, C_2H_6, and C_3H_8 as High as 97 bar," *Appl. Phys. B* **71**, 865-871, (2000).

[20] T. S. Cheng, T. Yuan, C.-C. Lu, and Y.-C. Chao, "The Application of Spontaneous Vibration Raman Scattering for Temperature Measurements in High Pressure Laminar Flames," *Combust. Sci. Technol.* **174**, 111-128, (2002).

[21] D. A. Long, *Raman Spectroscopy*, McGraw-Hill, London, (1977), CRS1-16.

[22] G. Hertzberg, *Molecular Spectra and Molecular Structure - I. Spectra of Diatomic Molecules*: 2nd Ed., Krieger Publishing Company, Florida, (1950), 66-141.

[23] K. P. Huber, and G. Hertzberg, *Molecular Spectra and Molecular Structure - IV. Constants of Diatomic Molecules*, Van Nostrand Reinhold Company, New York, (1979), 250.

[24] A. P. Thorne, *Spectrophysics*, Chapman and Hall, London, (1974), 255-285.

[25] F. Schreier, "The Voigt and Complex Error Function: A Comparison of Computational Methods," *J. Quant. Spectrosc. Radiat. Transfer* **48**, 743-762 (1992).

[26] J. Hussong, W. Stricker, X. Bruet, P. Joubert, J. Bonammy, D. Robert, X. Michaut, T. Gabard, H. Berger, "Hydrogen CARS Thermometry in H_2-N_2 Mixtures at High Pressure and Medium Temperatures: Influence of Linewidths Models," *Appl. Phys. B* **70**, 447-454, (2000).

[27] J. Hussong, R. Lückerath, W. Stricker, X. Bruet, P. Joubert, J. Bonammy, and D. Robert, "Hydrogen CARS Thermometry in High-Pressure H_2-Air Flame. Test of H_2 Temperature Accuracy and Influence of Line Width by Comparison with N_2 CARS as Reference," *Appl. Phys. B* **73**, 165-172, (2001).

[28] B. J. McBride, and S. Gordon, "Computer Program for Calculation of Complex Chemical Equilibrium Compositions and Applications – II. Users Manual and Program Description," NASA RP-1311, (1996),

[29] A. Lévy, N. Lacome, and C. Chackerian, "Collisional Line Mixing," in *Spectroscopy of the Earth's Atmosphere and Interstellar Medium*, Academic Press, San Diego, (1992), 261-422; and references therein.

[30] F. Rabenstein, and A. Leipertz, "Two-Dimensional Temperature Determination in the Exhaust Region of a Laminar Flat-Flame Burner with Linear Raman Scattering," *Appl. Opt.* **36**, 6989-6996, (1997).

[31] S. M. Schoenung, and R. E. Mitchell, "Comparison of Raman and Thermocouple Temperature Measurements in Flames," *Combust. Flame* **35**, 207-211, (1979).

[32] M. C. Drake, and G. M. Rosenblatt, "Rotational Raman Scattering from Premixed and Diffusion Flames," *Combust. Flame* **33**, 179-196, (1978).

[33] W. G. Breiland, M. E. Coltrin, and P. Ho, "Comparisons between a Gas-Phase Model of Silane Chemical Vapor Deposition and Laser-Diagnostic Measurements," *J. Appl. Phys.* **59**, 3267-3273, (1986).

[34] Y. Gu, E. W. Rothe, and G. P. Reck, "One-Dimensional Imaging of H_2 Densities and of Temperatures via Rotational Raman Scattering of Narrow-Band, 248 nm, Laser Light," *J. Raman Spectrosc.* **28**, 605-612, (1997).

[35] T. X. Phuoc, "Laser Spark Ignition: Experimental Determination of Laser-Induced Breakdown Thresholds of Combustion Gases," *Opt. Communications* **175**, 419-423, (2000)

[36] F. Grisch, P. Bouchardy, W. Clauss, "CARS Thermometry in High Pressure Rocket Combustors," *Aeros. Sci. Technol.* **7**, 317-330 (2003).

[37] K. L. McNesby, and J. B. Morris, "Fourier Transform Raman Spectroscopy of Nitrogen at High Pressure," *J. Raman Spectrosc.* **26**, 487-490, (1995).
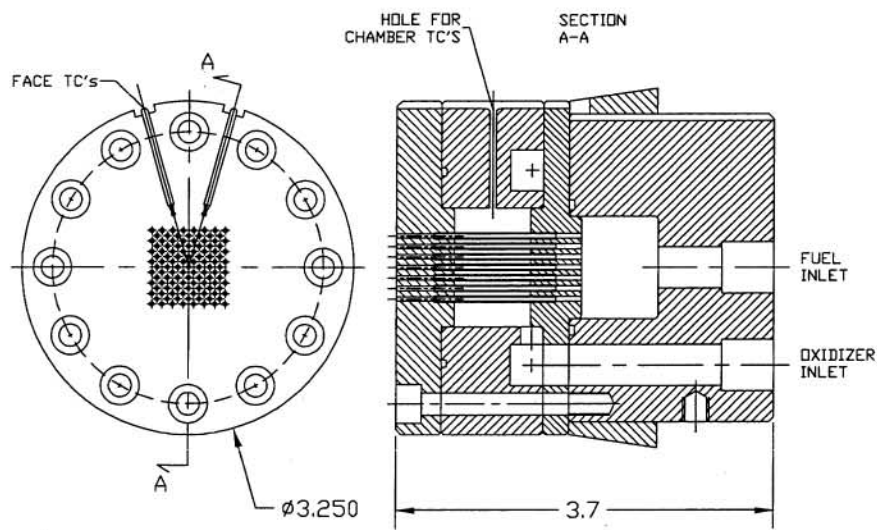
Figure 1: Schematic of multi-tube burner nozzle to provide a quasi-premixed flame at high pressures. *Left*: top view, *Right*: side view (cross-section diagram). Units are in inches.
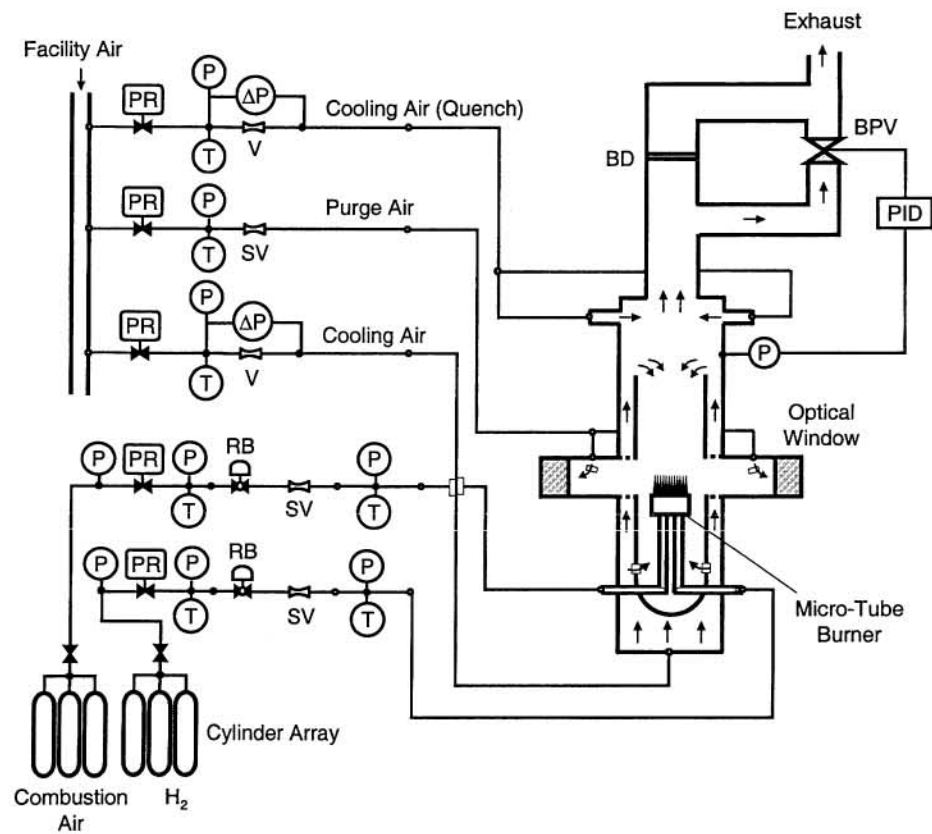
Figure 2: Schematic of high-pressure gaseous burner facility flow systems. Legends - P: pressure transducer; T: thermocouple; PR: remotely operated regulator; RB: remotely operated ball valve; V: venturi; SV: sonic venturi; BPV: back-pressure valve; PID: process controller; BD: burst disk.
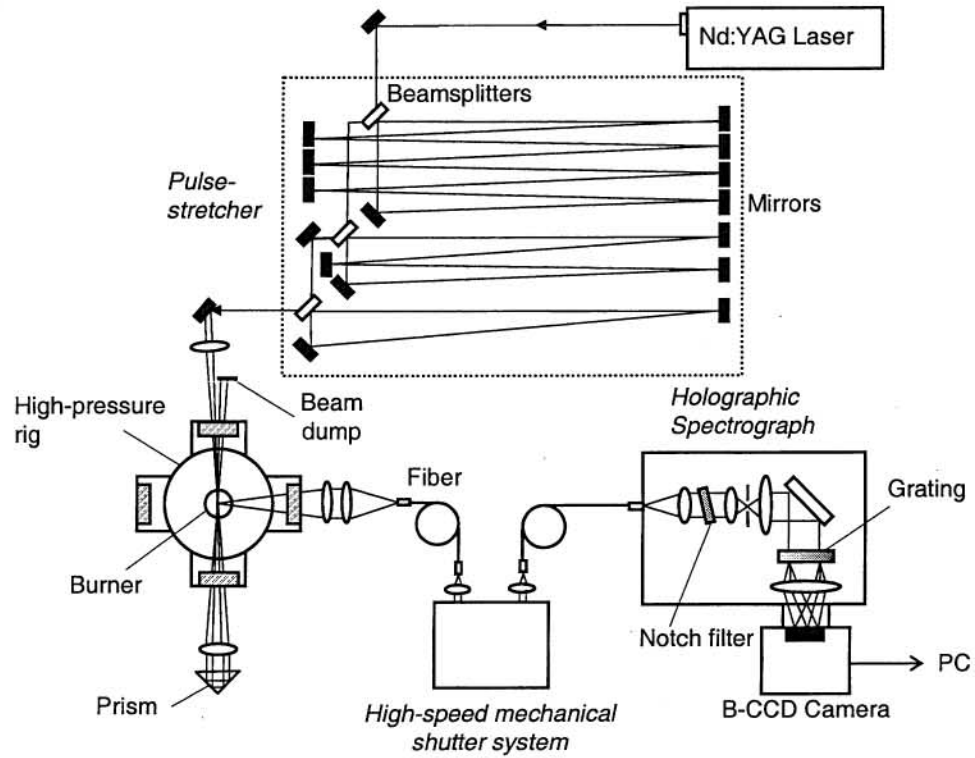
Figure3: Schematic of high-performance Raman scattering apparatus. There are 4 main components to the system: Nd;YAG laser, pulse-stretcher, high-speed shutter (24 microsecond gate), and spectrograph/backside-illuminated CCD camera.
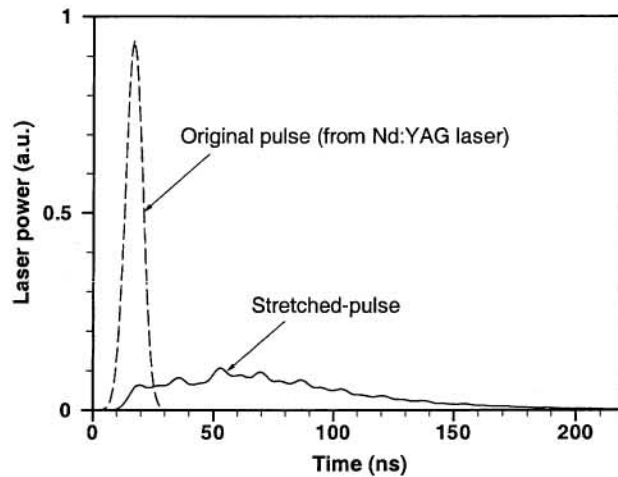
Figure 4: Measured (256-shot average) temporal profile of excitation laser pulse demonstrating the performance of the pulse-stretcher. Using an optimized 3-cavity pulse-stretcher, an original laser pulse is stretched out in time and reduced to 10% of original peak power with an 83% throughput efficiency.
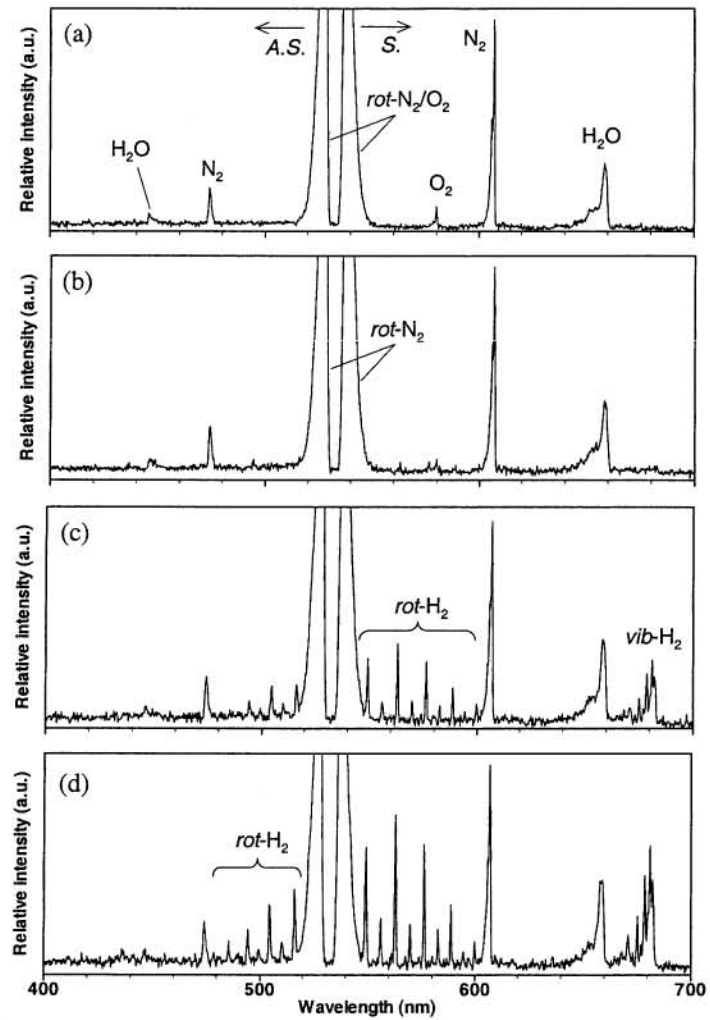
Figure 5: Measured Raman spectra in 10-atm H_2/air combustion gases (700-shot average). Background flame luminescence has been subtracted. (a) $\phi = 0.5$, (b) $\phi = 1.0$, (c) $\phi = 2.0$, (d) $\phi = 3.0$. *A.S.* and *S.* indicate anti-Stokes and Stokes band, respectively. *rot-* and *vib-* indicate pure rotational and vibrational scattering, respectively. Rayleigh scattering light at 532 nm has been eliminated by a narrow-band Notch filter around.
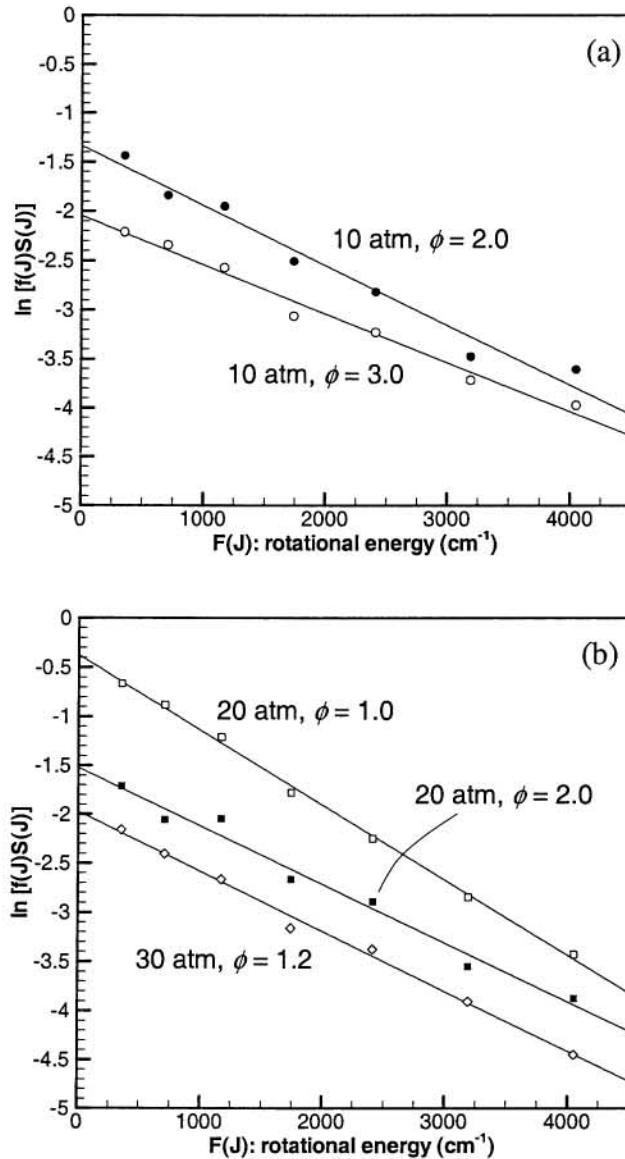
Figure 6: Rotational temperature determination plots based on pure rotational H_2 Raman spectra in high-pressure, fuel-rich hydrogen flames. (a) 10-atm flames, (b) 20-atm, and 30-atm flames. Only Stokes branches ($J = 2$ to 8) are used here for temperature calculations. Solid lines are non-intensity weighted, linear least-squares fits. Uncertainties of these fits provide temperature uncertainties shown in Table 1.

Table 1: Experimentally derived temperatures and their uncertainties for various high-pressure H_2 flames. Uncertainty is calculated from the standard deviation of the slope of the linear fit to the plots in Fig. 6.

| Case	#1	#2	#3	#4	#5
P (atm)	10	10	20	20	30
ϕ	2.0	3.0	1.0	2.0	1.2
$T_{rot}(H_2)$	2467 ± 67	2234 ± 79	2443 ± 74	1878 ± 19	2355 ± 38
$\sigma(\%)$	2.7	3.6	3	1	1.6
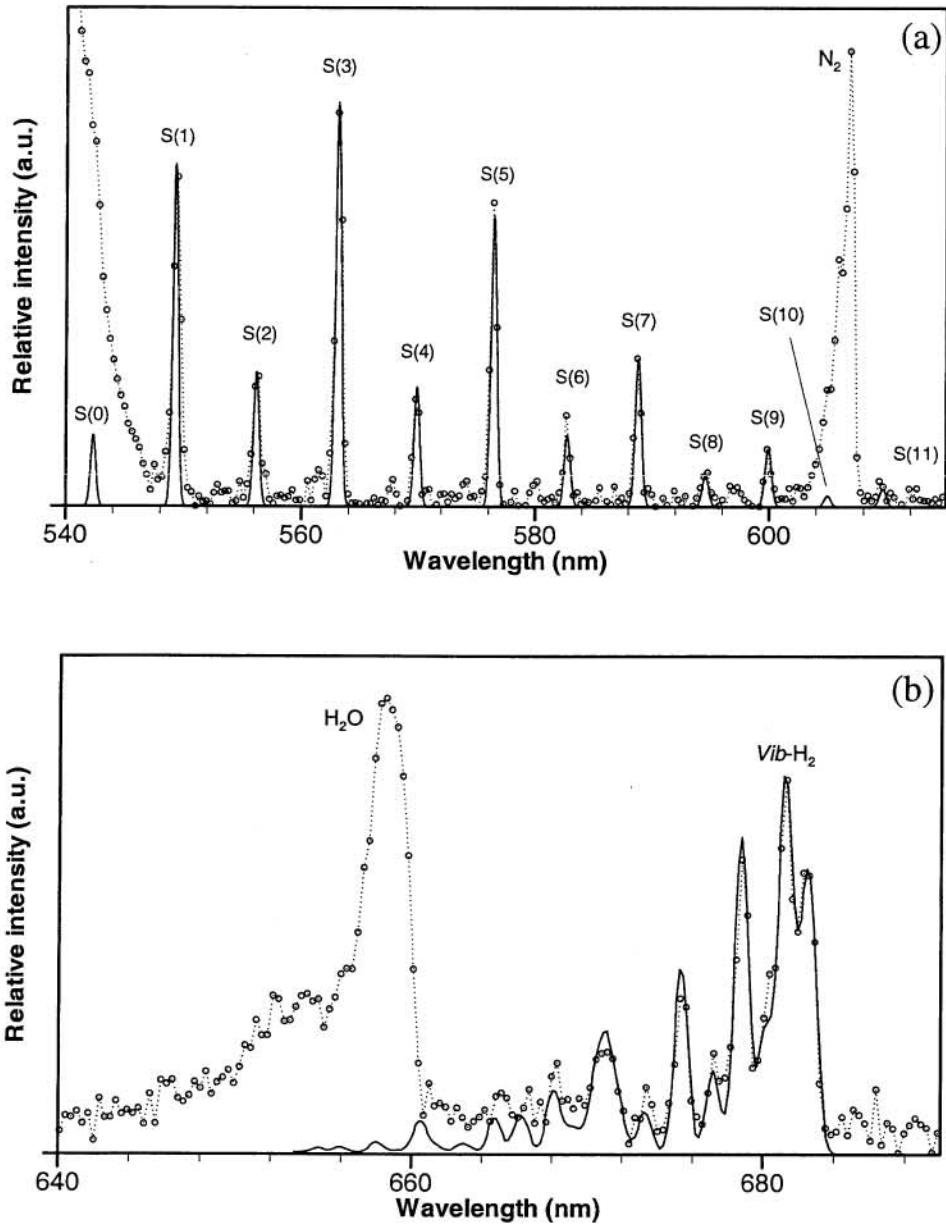
Figure 7: Fine structure of Raman spectra in high-pressure H_2 flames at 10 atm, $\phi = 3.0$. (a) Rotational H_2 spectra and N_2 Q-branch. (b) Vibrational H_2 and vibrational H_2O. *Dot* is experiment, *Line* is theoretical calculation at 2234 K. 700-shot average.
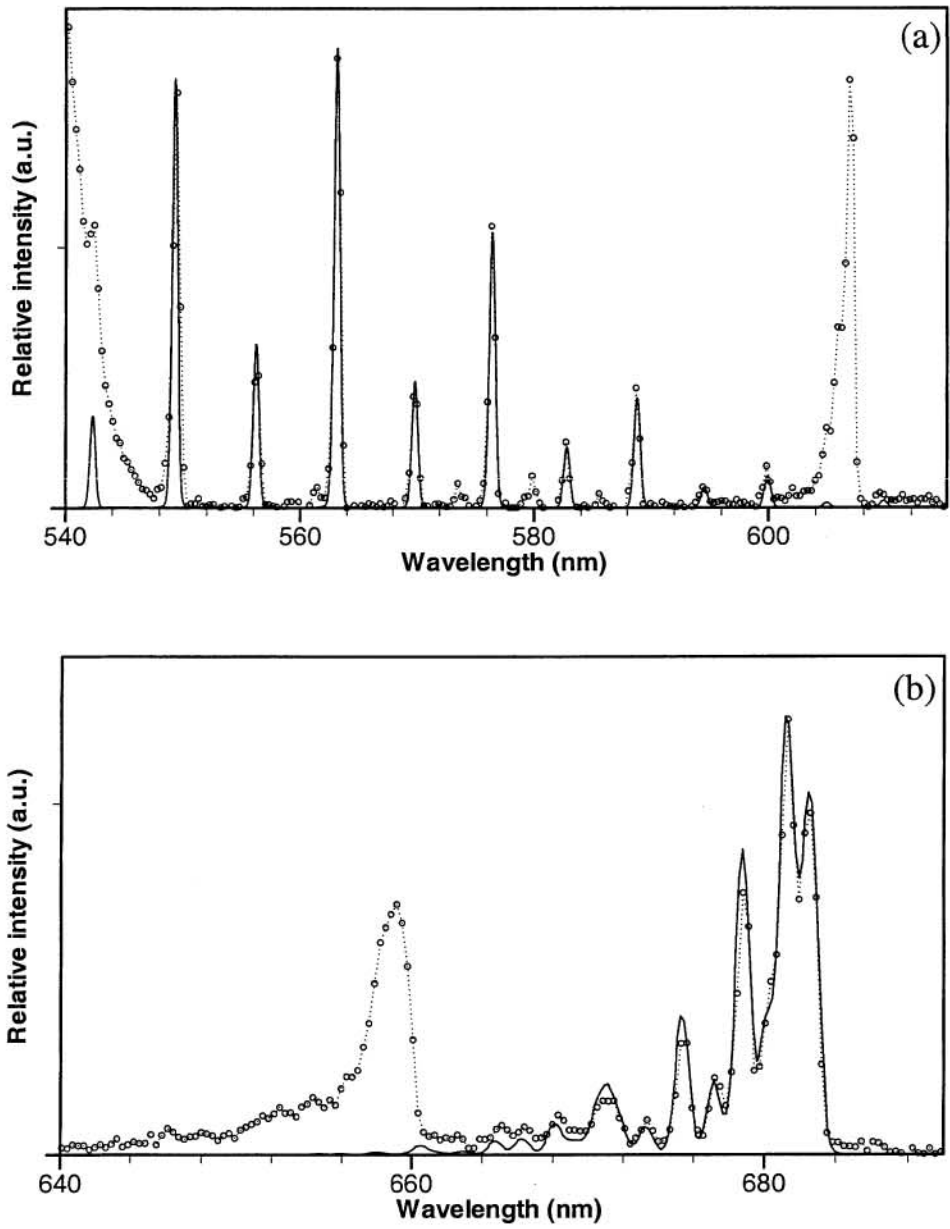
Figure 8: Fine structure of Raman spectra in high-pressure H_2 flames at 20 atm, $\phi = 2.0$. (a) Rotational H_2 spectra and N_2 Q-branch. (b) Vibrational H_2 and vibrational H_2O. *Dot* is experiment, *Line* is theoretical calculation at 2443 K. 700-shot average.
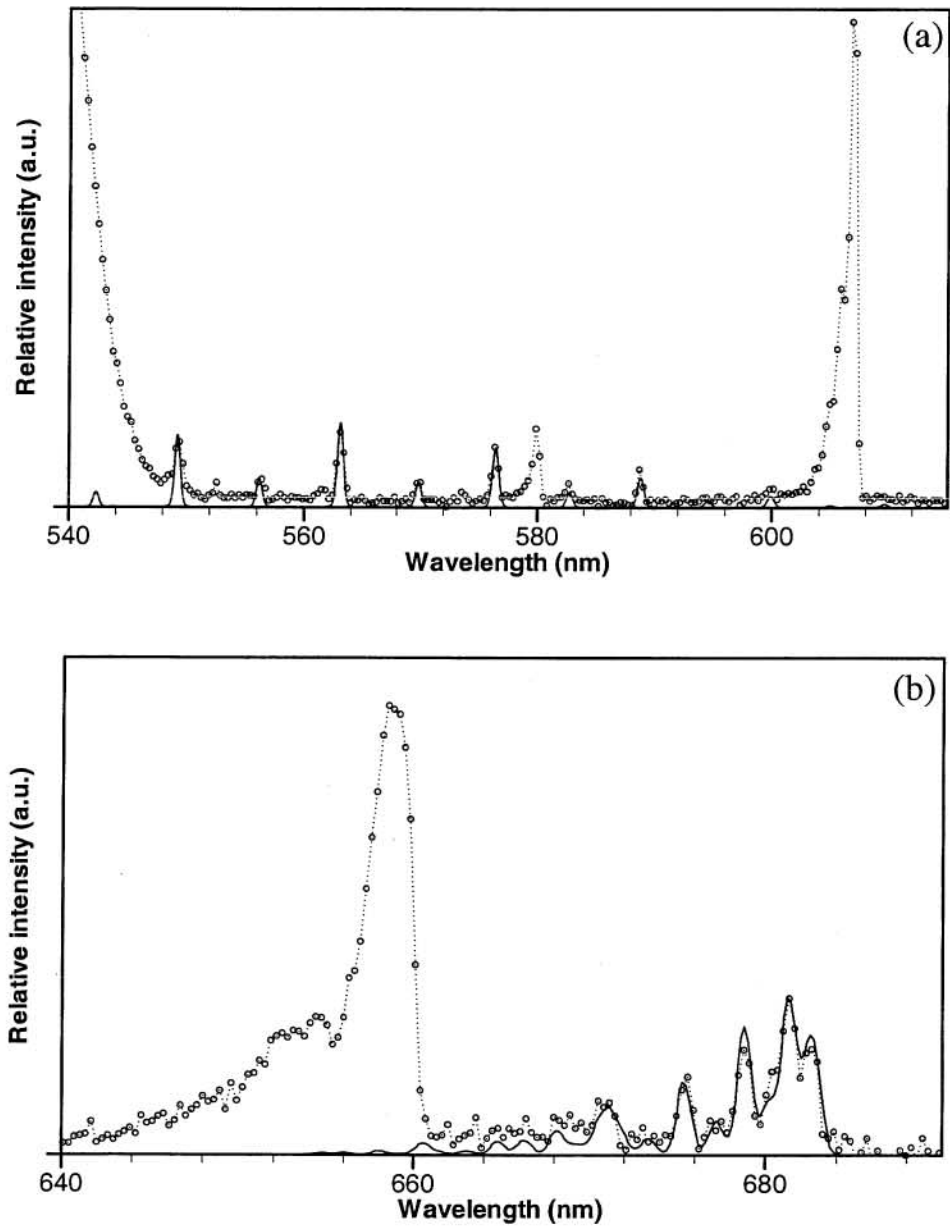
Figure 9: Fine structure of Raman spectra in high-pressure H_2 flames at 30 atm, $\phi = 1.2$. (a) Rotational H_2 spectra and N_2 Q-branch. (b) Vibrational H_2 and vibrational H_2O. *Dot* is experiment, *Line* is theoretical calculation at 2355 K. 700-shot average. Vibrational O2 spectrum is observed because of residual oxygen.
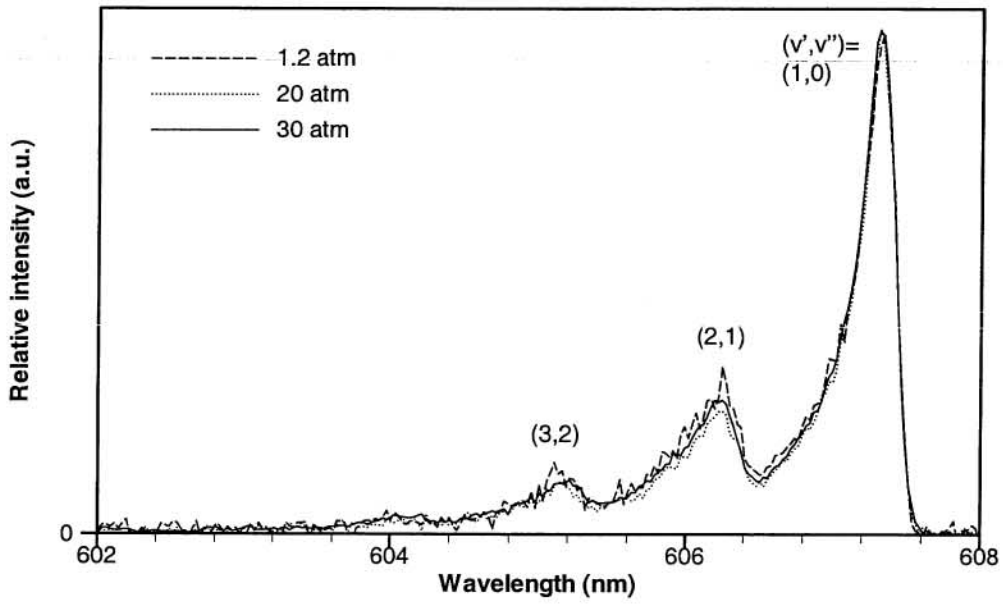
Figure 10: Vibrational Q-branch of N_2 Raman spectra in low- and high-pressure H_2 flames ($\phi = 0.5$). 600-shot average. Data obtained using high-dispersion grating.